Journal of Applied Physics

RESEARCH ARTICLE | MAY 20 2026

Estimation of electron mobility in the hollow cathode plume of a Hall effect thruster with different electrical configurations

Special Collection: Impact of Vacuum Facilities on Plasma Thruster Operation

Yusuke Yamashita ; Naia Butler-Craig ; Mitchell L. R. Walker ; Kentaro Hara

J. Appl. Phys. 139, 193305 (2026)
https://doi.org/10.1063/5.0316910

Journal of Applied Physics ARTICLE pubs.aip.org/aip/jap

Estimation of electron mobility in the hollow cathode plume of a Hall effect thruster with different electrical configurations

Cite as: J. Appl. Phys. **139**, 193305 (2026); doi: 10.1063/5.0316910
Submitted: 16 December 2025 · Accepted: 28 April 2026 ·
Published Online: 20 May 2026

Yusuke Yamashita,[1,a)] Naia Butler-Craig,[2] Mitchell L. R. Walker,[2] and Kentaro Hara[1]

AFFILIATIONS

[1]Department of Aeronautics and Astronautics, Stanford University, Stanford, California 94305, USA
[2]School of Aerospace Engineering, Georgia Institute of Technology, Atlanta, Georgia 30332, USA

Note: This paper is part of the Special Topic on Impact of Vacuum Facilities on Plasma Thruster Operation.
[a)]**Author to whom correspondence should be addressed:** yamashita.yusuke@jaxa.jp

ABSTRACT

In the paper, we assess the effects of electrical configuration on the plasma properties in the near-field hollow cathode discharge that is center mounted on a Hall effect thruster. The axial profile of the electron density and temperature is obtained using incoherent laser Thomson scattering for three electrical configurations of the thruster body, i.e., grounded, floating, and cathode-tied. The effective electron mobility is estimated using a one-dimensional plasma fluid model with the measurement data as an input to the model. The estimation using the data-driven framework reveals that the electron conductivity is the highest when the thruster body is electrically grounded while the electron conductivity is comparable between the floating and cathode-tied configurations, indicating that the current path and electron dynamics of the hollow cathode discharge are affected by the electrical configurations.

I. INTRODUCTION

Electric propulsion (EP) systems have recently been developed for various space missions, including deep space missions[1–4] and Earth orbit missions.[5,6] When developing EP devices, they are tested in ground facilities, i.e., vacuum chambers, to measure the thrust performance and lifetime.[7–10] However, differences in thruster operation have been identified between in-space operations and ground-based measurements, e.g., performance and lifetime, for various EP systems, such as Hall effect thrusters (HETs)[11,12] and gridded ion thrusters (GITs).[1,13] The differences between in-space operation and ground-based tests are attributed to the so-called facility effects.[14,15]

The facility effects are mainly divided into three categories: background pressure in the facility, i.e., pressure effects, contamination of hardware as a result of sputtered materials from the facility walls, i.e., contamination effects, and the electrical conductivity through the testing facility, i.e., the electrical effect. For the background pressure effects, the thrust,[16] oscillation amplitude of the discharge current,[17] and plasma properties, e.g., ion bulk velocity,[18,19] can be affected by the residual background gas entering the HET. Charge exchange (CEX) collisions can modify the divergence angle of the ion beams[20] and may change the current paths.[21] A recent work of the data-assimilation suggests that the time-dependent plasma properties are also affected by the background pressure.[15] For the contamination effects, the ion beam sputters the beam dump or vacuum chamber walls and the sputtered materials deposit on thruster surfaces.[22–24] This may cause differences in the thrust performance and lifetime evaluation between in-space and ground-based operations.[1,22]

For electrical facility effects, additional current paths from the thruster body to the chamber electrical ground and from the plasma plume to the vacuum chamber wall may affect the thruster and cathode performance.[21,25] For instance, a GIT ground-based test suggests that the electrical connection of the thruster cover to the chamber ground affects the cathode-to-ground voltage.[26] The loss of electrically conducting surfaces due to sputtering of the covered material, e.g., indium tin oxide-coated silver fluorinated ethylene propylene film,[27] is hypothesized to be one of the main causes for the increase in cathode voltage during space operation.[28] In HETs, the electrical configuration of the thruster body can be connected to the electrical ground, floating, or cathode-tied.[29,30] Several experimental works suggest that the thrust,[29] mean discharge current,[31] and discharge current oscillations[21,25,29,30] are affected by the electrical configurations. Notably, Ref. 29 shows that the choice of the dielectric material, e.g., Al_2O_3, and the conducting material, e.g., graphite, used in the thruster body also plays an important role in thruster performance. In addition, Ref. 21 analyzes the current path from the plasma plume to the vacuum chamber wall. An impedance analysis shows that the plasma sheath near the vacuum chamber walls may yield a capacitive or inductive effect depending on the frequency.[21,32]

In this paper, we investigate electrical facility effects on the near-field discharge plasma of a hollow cathode, which is center mounted on in the H9 thruster.[33] Incoherent laser Thomson scattering is used to measure the electron density and electron temperature in the near-field of the cathode for three different electrical configurations: grounded, floating, and cathode-tied.[30] The experimental data are input into a one-dimensional (1D) plasma fluid model, and the electron mobility is estimated through a model-data fusion framework. This study elucidates how the near-field electron transport, which plays a role for the thruster performance, is affected by the electrical configuration of the thruster body. Section II introduces the experimental conditions and data obtained from the incoherent laser Thomson scattering. Section III explains the fluid model of the hollow cathode plasma and explains the unknown parameters that are estimated. Section IV shows the estimated plasma properties and discusses the electrical facility effects.

II. EXPERIMENTAL CONDITIONS AND MEASUREMENT DATA

The H9 thruster[33] is operated with an input power of 6 kW, where the discharge voltage is 300 V and the discharge current is approximately 20 A, in the VTF-2 vacuum chamber at Georgia Institute of Technology. The working gas is krypton. The anode and cathode mass flow rate are 14.35 and 1.26 mg/s, respectively, for all electrical configurations.

A. Hollow cathode operation

The hollow cathode is mounted at the center of the H9.[30] Figure 1 shows the schematics of the hollow cathode and HET. The discharge power supply is electrically isolated from the ground. For the H9 thruster, the surface of the thruster body is graphite, i.e., a conductive material; thus, the thruster body voltage can be biased. Typically, the cathode voltage is lower than the electrical ground, which is characterized by the cathode-to-ground voltage, i.e., V_{cg}. Let the thruster body voltage with respect to the ground be V_{tb}. In the experiment, the H9 is operated in three electrical configurations as shown in Fig. 1: (a) grounded ($V_{tb} = 0$ V), (b) floating ($V_{tb} = V_{tb,f}$), and (c) cathode-tied ($V_{tb} = V_{cg}$). In this experiment, it was observed that $V_{cg} \approx -15$ V for all three electrical configurations. In addition, the thruster body voltage for the floating configuration is $V_{tb} = V_{tb,f} \approx -20$ V, which is more negative than V_{cg}, where $V_{tb,f}$ is the floating voltage of the thruster body with respect to the ground. The negative V_{tb} indicates that ions, e.g., due to CEX collisions, are attracted to the thruster body and the electron current is adjusted by the sheath around the thruster body to achieve net zero current collection in the floating configuration.[29,30,34,35] In addition, this implies that in the cathode-tied configuration, i.e., V_{tb} is more negative than V_{cg}, the thruster body is slightly electron current repelling, if the plasma condition around the thruster body is not altered by the electrical configuration.

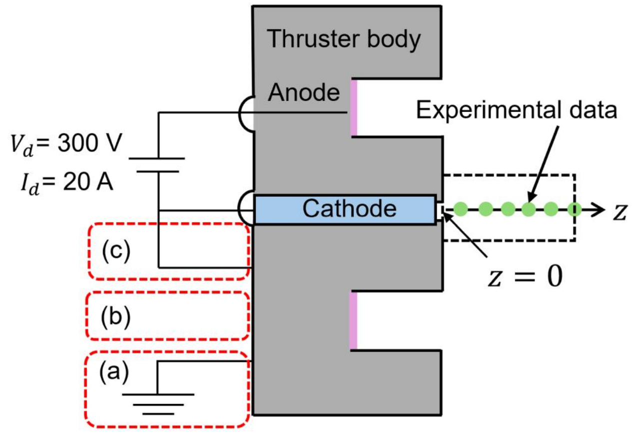

FIG. 1. Schematic of a HET with a center-mounted hollow cathode. Axial profile of n_e and T_e obtained from the incoherent laser Thomson scattering[30] is used for the estimation of electron mobility. The testing was performed with three different electrical configurations: (a) grounded, (b) floating, and (c) cathode-tied. The discharge power supply is electrically isolated from the ground. $z = 0$ mm is defined at the axial position of the thruster body surface.

The discharge current was measured at current shunt lines at the back of the power rack in the control room. A Teledyne LeCroy CP150 current probe is clamped to the anode electrical line to acquire time-resolved measurements of the discharge current. The sampling rate and total recording time of the discharge current were 1 MHz and 1 s, respectively. The discharge current for the grounded, tied, and floating configuration averaged 19.6, 20.0, and 20.1 A, respectively.

Figure 2 shows the power spectral density (PSD) of the discharge current oscillation in the three electrical configurations: grounded, floating, and cathode-tied. We obtain the PSDs from the raw discharge current data, and then a 64-point running average is applied to the PSDs in the frequency domain. The dominant frequencies of the discharge current oscillation are 14.1, 15.2, and 18.1 kHz for the floating, cathode-tied, and grounded configurations, respectively. The amplitude of the discharge current oscillation is smallest for the grounded configuration, while the amplitude is comparable between the floating and cathode-tied configurations. The root mean square (RMS) of the discharge current is 0.898, 1.38, and 1.63 A for the grounded, tied, and floating configurations, respectively. It should be noted that in the NASA Hall Effect Rocket with Magnetic Shielding (HERMeS), operating at 12.5 kW, the trend of the discharge current amplitude

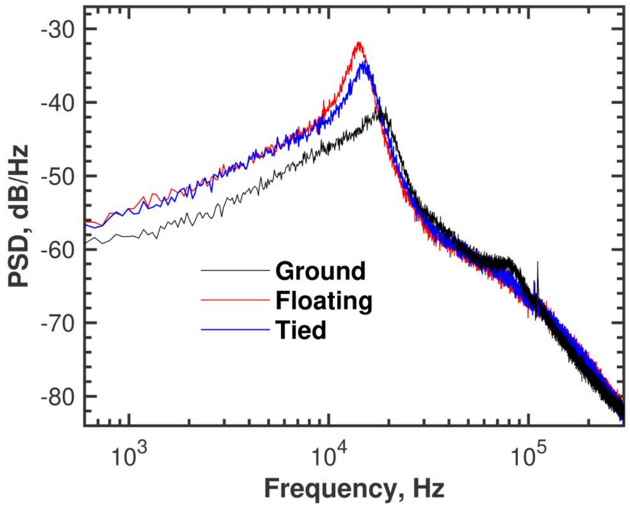

FIG. 2. Power spectral density (PSD) of discharge current oscillation in different electrical configurations: grounded, floating, and cathode-tied.

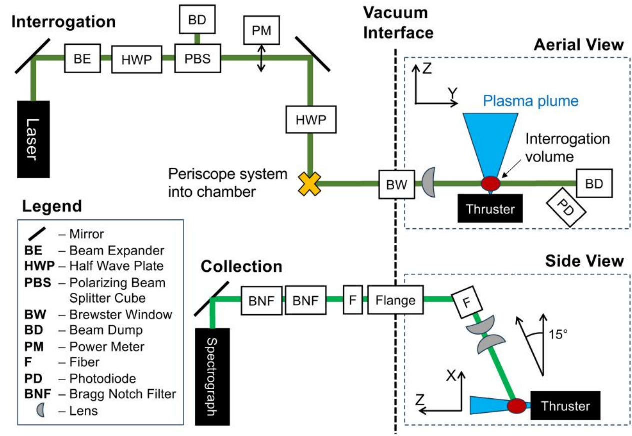

FIG. 3. Setup for laser Thomson scattering (LTS), including the interrogation, collection, and detection systems (adapted fromButler-Craig *et al.*, Comparison of the near-field electron properties of the H9 Hall effect thruster in various electrical congurations with incoherent laser Thomson scattering," in AIAA SCITECH 2025 Forum, No. AIAA-2025-1099 (AIAA, 2025).[30] Copyright 2025 American Institute of Aeronautics and Astronautics, Inc.

at the dominant frequency is consistent with this study. However, a different trend in the dominant frequency itself is observed for both thruster bodies covered by the dielectric material, e.g., Al_2O_3, and conducting material, e.g., graphite:[29] The dominant frequency was lowest for the grounded configuration, highest for the floating configuration, and intermediate for the cathode-tied configuration. The main difference is that this study fixes the total mass flow rate, whereas the total mass flow rate was adjusted to keep the discharge power constant in Ref. 29.

B. Incoherent laser Thomson scattering

An incoherent laser Thomson scattering (LTS) has been developed[36–38] to measure the electron density, n_e, and the electron temperature, T_e. An Amplitude DLS Powerlite 9010 injection-seeded Nd:YAG laser, operating at the second harmonic wavelength of 532 nm, delivered a beam diameter of 9 mm. The laser pulse duration ranged between 5 and 8 ns, with a maximum energy output of 1.15 J/pulse with a 10 Hz repetition rate. However, due to the misalignment internal to the laser, the maximum laser outputted around 670 mJ/pulse. The optical beam path depicted in Fig. 3 is as follows. The beam exits the laser and turns into a beam expander (BE) assembly and then into a half-wave plate (HWP) and polarizing beam splitter (PBS) cube so that the laser energy could be modulated without changing the timing settings internal to the laser. The energy was averaged over the 2.5-min acquisition duration and measured by a Gentec UP52N-50S-QED-D0 power meter (PM), enabling quick and unobtrusive energy measurements between LTS acquisitions. The beam goes through another HWP that determines the final polarity of the beam before it enters the vacuum chamber through the periscope and Brewster window (BW). The beam waist of about 100 μm intersects with the interrogation volume 2 mm downstream of the thruster face through a 600 mm focal length lens inside the chamber. The scattered light is collected and transmitted through two custom Thorlabs FG200LEA-FBUNDLE fiber bundles that contain seven 200 μm FG200LEA multimode fibers. The two fiber bundles were connected in series through a flange allowing for the collected light at the thruster to be relayed out of the chamber and into the external collection system. The light relayed through the bundles was spectrally filtered through two Optigrate OD-4 Bragg Notch Filters (BNFs) and then delivered to the spectrograph. The spectrograph consists of a Princeton Instruments ISOPLANE-320A spectrometer and a PM4-1024i-HB-FG-18-P46 PIMAX4 camera.[30] The collection fibers are aligned to account for chamber compression from the atmosphere to high vacuum. To enable this, the internal fiber bundle was placed on three motorized stages. Fine alignments at the axial location nearest to the cathode centerline are also made between each measurement to ensure that the maximum signal at the start of the experiment could be recovered throughout. For further details on the optical system design and alignment, refer to Ref. 38.

The electron properties were obtained by fitting the measured Thomson spectra. Prior to analysis, the collection instruments were intensity-calibrated using laser Raman scattering (LRS) in air, where the synthetic spectra of N_2 and O_2 were fitted to determine the transmission efficiency fo the detection branch. In the present experiment, the electron density and temperature are measured along the centerline of the hollow cathode in the near-field plume between $z = 1.75$ mm and $z = 17.75$ mm in three electrical configurations: grounded, floating, and cathode-tied.[30] Here, $z = 0$ mm corresponds to the thruster surface shown in Fig. 1. The axial resolution is 2 mm. For each spatial location, the Thomson scattering signal, S_{Th}, was determined as

$$S_{Th} = S_{raw} - (S_{emi} + S_{ref} + S_{back}), \tag{1}$$

where S_{raw} is the raw Thomson signal (laser and plasma on), S_{emi}

is the signal due to plasma emission (laser off), S_{ref} is the signal due to laser reflections (plasma off), and S_{back} is the background signal (laser and plasma off). In this study, the LTS spectra were time-averaged over 1500 shots (corresponding to 2.5 min) to improve the signal-to-noise ratio.

Electron properties, such as the electron density n_e and electron temperature T_e, were estimated from the measured Thomson spectra by assuming a Maxwellian distribution with an electron bulk velocity $u_{e,s}$ along the scattering vector,

$$f(v_{e,s}) = n_e\sqrt{\frac{m_e}{2\pi k_B T_e}}\exp\left\{-\frac{m_e(v_{e,s}-u_{e,s})^2}{2k_B T_e}\right\}, \tag{2}$$

where m_e is the electron mass and k_B is the Boltzmann constant. It should be noted that the Thomson signal is not available near $v_{e,s} \approx 0$ due to filtering by BNFs. Therefore, the Maxwellian fitting was performed using only the LTS data, excluding the region around $v_{e,s} \approx 0$. The uncertainties in electron number density and electron temperature are estimated from the 95% confidence bounds of the fit.

C. LTS spectra

Figure 4 shows the LTS spectra S_{Th} at $z = 1.75$ mm in the cathode-tied configuration: (a) electron velocity distribution function (EVDF) and (b) electron energy distribution function (EEDF). $v_{e,s}$ is obtained from the Doppler shift as

$$v_{e,s} = \frac{c(\lambda - \lambda_l)}{2\lambda_l \sin(\theta/2)}, \tag{3}$$

where c is the light speed, λ_l is the wavelength of laser, and θ is the angle between the laser injection and spectra detection. In this study, $\theta = 90°$ and $\lambda_l = 532$ nm are used. Figures 4(a) and 4(b) indicate that the Maxwellian assumption is reasonably valid. From the Maxwellian fitting, the electron density, temperature, and bulk velocity along the scattering vector are estimated as $n_e \approx 1.0 \times 10^{19}\ \mathrm{m^{-3}}$, $T_e \approx 2.7$ eV, and $u_{e,s} \approx 4.1 \times 10^4$ m/s, respectively. As shown in Fig. 4(b), the asymmetry of the LTS spectra between $v_{e,s} > 0$ and $v_{e,s} < 0$ is attributed to the finite bulk velocity $u_{e,s}$. It should be noted that the raw LTS spectra contain a slight offset, as seen in Fig. 4(b), due to the error in the subtraction procedure described in Eq. (1). This offset is therefore included as a fitting parameter in the Maxwellian fitting.

The scattering vector is given by $k_s = k_d - k_l$, where k_l is the laser direction and k_d is the detection direction. From the experimental configuration shown in Fig. 3, the scattering vector is inclined by $\chi_s \approx 10.5°$ from z axis in the $r-z$ plane, where $r = \sqrt{x^2+y^2}$. Assuming $u_{e,r} \approx 0$, $u_{e,z} \approx u_{e,s}/\sin\chi_s \approx 1.6 \times 10^5$ m/s. However, although the order of $u_{e,z}$ may be reasonable, this estimation of $u_{e,z}$ is highly sensitive to uncertainties in $u_{e,s}$ because the scattering angle relative to z axis is small. In addition, several previous studies suggest that the estimation of $u_{e,s}$ is challenging for LTS measurement[39] due to the lack of reliable data near $v_{e,s} \approx 0$ shown in Fig. 4(a), where the electron Mach number is $M_{e,s} \ll 1$. Therefore, in this study, $u_{e,z}$ is primarily estimated using a fluid model, as discussed later.

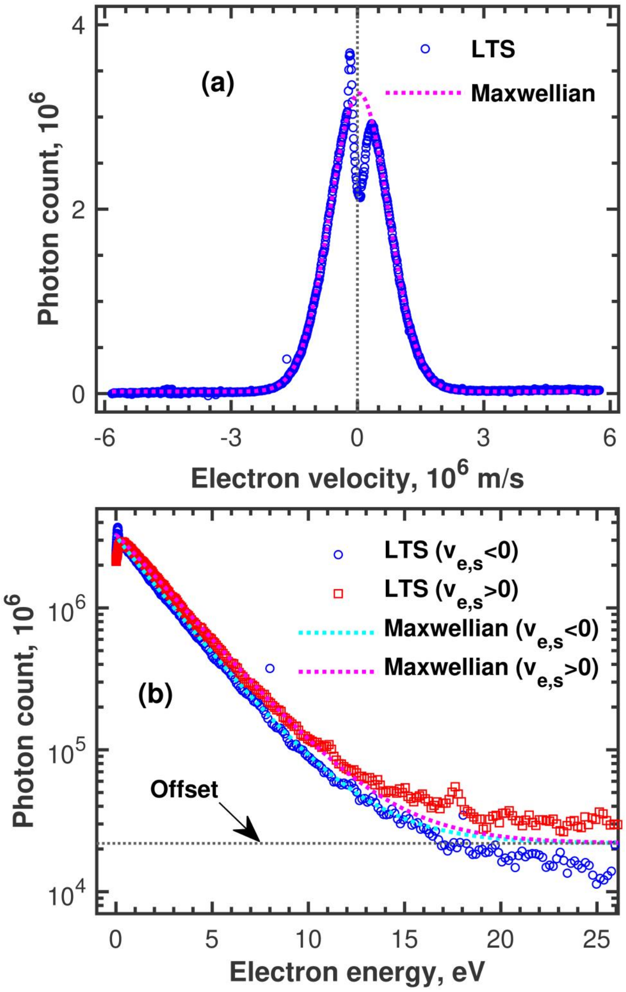

FIG. 4. Experimental data of LTS spectra and Maxwellian fitting. (a) Electron velocity distribution function (EVDF). (b) Electron energy distribution function (EEDF). Symbol: experimental data, dashed line: Maxwellian fitting. A small offset, arising from uncertainties in the background subtraction in Eq. (1), is included in the fitting procedure.

D. Experimental data of n_e and T_e

Figure 5 shows the measured electron properties, i.e., (a) $n_e(z)$ and (b) $T_e(z)$, for three electrical configurations. Symbols show the experimental data of n_e and T_e obtained from the LTS measurement. Figure 5(a) shows that n_e decreases most rapidly in the plume in the grounded configuration. In addition, Fig. 5(b) shows that T_e is the highest for the floating configuration and lowest for the grounded configuration. It should be noted that in the cathode-tied configuration, n_e exhibits a slight increase at $z = 3.75$ mm compared to $z = 1.75$ mm. A relatively higher n_e at $z = 3.75$ mm, compared with the floating and grounded configurations, is also observed at a discharge current of 40 A.[40] In this study, the keeper voltage $V_k \approx 7-8$ V across all electrical

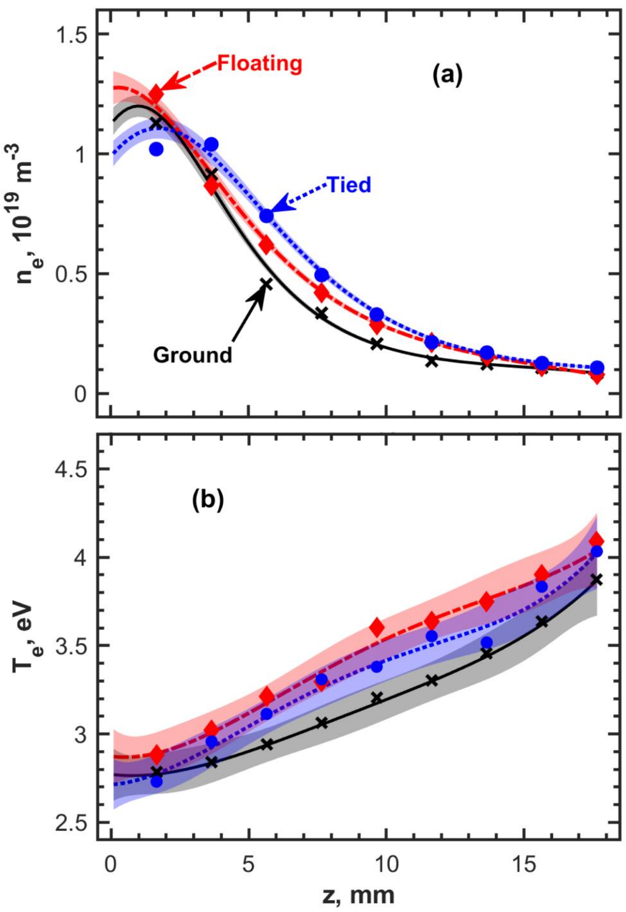

FIG. 5. Data used for the model-data fusion framework: (a) n_e and (b) T_e for three electrical configurations: grounded, floating, and cathode-tied. Symbols: measurement data obtained from the incoherent laser Thomson scattering (LTS).[30] Solid line: mean value of the polynomial fitting. Shadow region: ±2σ of the polynomial fitting. In this study, an experimental uncertainty of $\pm 5\%$ is used for each data point, and then the polynomial fitting is performed.

configurations. In the cathode-tied configuration, since $V_{cg} = V_{tb} < V_k$, a local potential hump forms near the keeper, which may contribute to the observed increase in n_e. A detailed understanding of the underlying mechanism is beyond the scope of the present study and reserved for future work.

In this study, the uncertainty of experimental data is treated based on the Monte Carlo sampling. We consider the uncertainty of experimental data with a uniform distribution of $\pm$ 5% for both n_e and T_e, which is approximately the maximum error bar of the LTS data.[30] For one sample of the state estimation, data are considered at the discrete locations where measurements are taken using a uniformly distributed random number. Using the randomly sampled data, a polynomial fitting is performed through the sampled data to obtain smooth profiles of n_e and T_e. It should be noted that n_e and T_e at $z = 0$ mm are required to provide the boundary conditions for the state estimation, as discussed later. While the electron density may be larger at $z = 0$ mm, other results, such as the cathode-tied configuration shown in Fig. 5, suggest that the axial variation near this region can depend on the operating or electrical conditions. In the absence of direct measurements at $z = 0$ mm in the present study, n_e and T_e at $z = 0$ mm are taken to be equal to those at the nearest measured location, $z = 1.75$ mm, as a first-order approximation. It is to be noted that the estimated properties, e.g., electron mobility, are locally affected by how n_e and T_e between $z = 0$ mm and $z = 1.75$ mm are assigned, but the overall structure of the estimated plasma properties was not affected by this treatment.[41]

The sampling procedure of n_e and T_e is repeated many times, e.g., 10^4, to obtain the statistics of the uncertain measurement data profiles that are used for the state estimation. The mean value and standard deviation, i.e., σ, are evaluated for $n_e(z)$ and $T_e(z)$. The solid line and shadow region in Fig. 5 show the mean value and $\pm 2\sigma$, respectively.

III. ESTIMATION OF ELECTRON TRANSPORT

The experimental data of n_e and T_e obtained from incoherent laser Thomson scattering, shown in Fig. 5, are input to a 1D fluid model of hollow cathode plasma to estimate the electron transport coefficients.

A. Physics-based model: An axial 1D fluid model

In this study, steady-state ($\partial/\partial t = 0$), quasi-neutral ($n_e = n_i$), and axial one-dimensional fluid equations for electrons, ions, and neutral are utilized for the estimation of hollow cathode plasma discharge. The neutral continuity equation is described as

$$\frac{d(n_n u_{n,z})}{dz} = -k_{iz} n_e n_n - \dot{n}_{\text{diff,n}}, \tag{4}$$

where n_n is the neutral density, $u_{n,z}$ is the axial neutral velocity, k_{iz} is the ionization rate, n_e is the electron density, $\dot{n}_{\text{diff,n}} = (n_n u_{n,r})/\Delta R$ denotes the radial diffusion rate, $u_{n,r}$ is the radial neutral velocity, and ΔR is the characteristics length of radial diffusion. Note that the ion recombination is neglected at the cathode exit. In this study, $\Delta R = 7$ mm is used, and $u_{n,r} = v_{th,n} = \sqrt{2k_B T_n/m_n}$, where $v_{th,n}$ is the neutral thermal speed, T_n is the neutral temperature, and m_n is the neutral mass. The ion continuity equation is described as

$$\frac{d(n_i u_{i,z})}{dz} = k_{iz} n_e n_n - \dot{n}_{\text{diff,i}}, \tag{5}$$

where n_i is the ion density (which is assumed to be equal to n_e), $u_{i,z}$ is the axial ion bulk velocity, $\dot{n}_{\text{diff,i}} = (n_i u_{i,r})/\Delta R$ is the radial diffusion for ions, and $u_{i,r}$ is assumed to be $u_{i,r} = u_{\text{B}} = \sqrt{kT_e/m_i}$, where u_{B} is Bohm velocity. It should be noted that only singly charged ions are considered in this study. The ion momentum equation is given by

$$m_i \frac{d\left(n_i u_{i,z}^2\right)}{dz} + \frac{d(n_i k_B T_i)}{dz} = e n_i E_z + m_i k_{iz} n_e n_n u_{n,z} - R_{\text{diff,i}}, \tag{6}$$

where $m_i \approx m_n$ is the ion mass, E_z is the axial electric field, T_i is the ion temperature, and $R_{\mathrm{diff,i}} = m_i \dot{n}_{\mathrm{diff,i}} u_{i,z}$ is the rate of change of momentum due to radial diffusion. The momentum drag due to ion-neutral collision is not considered for simplicity in this study. Considering no current in the radial direction, the current conservation across the cross-sectional plane at the cathode exit can be given by

$$I_d = e n_e A_p (u_{i,z} - u_{e,z}), \tag{7}$$

where I_d is the discharge current, $A_p = \pi(\Delta R)^2$ is the area of the plasma column, and $u_{e,z}$ is the axial electron velocity. Finally, using the drift-diffusion approximation where the electron inertia is neglected,[42] the electron flux is given by

$$n_e u_{e,z} = -\mu_{\mathrm{eff}} \left(n_e E_z + \frac{1}{e} \frac{\partial p_e}{\partial z} \right), \tag{8}$$

where $p_e = n_e k_B T_e$ is the electron pressure and μ_{eff} is the effective electron mobility that can be described as

$$\mu_{\mathrm{eff}} = \frac{e}{m_e(\nu_m + \nu_{ano})}, \tag{9}$$

which includes electron-neutral momentum transfer collision frequency, ν_m, and anomalous scattering frequency, ν_{ano}. The electron-neutral momentum transfer collision frequency can be written as $\nu_m = n_n k_m$, where k_m is the momentum transfer collision rate coefficient, including elastic collision and inelastic collision. Assuming the electron energy distribution function (EEDF) is Maxwellian, which is often used in the fluid simulations of EP plasmas, the rate coefficients of ionization, k_{iz}, and momentum transfer collision, k_m, can be tabulated as functions of electron temperature. In this study, Biagi-v7 data are used as the cross section of electron-neutral collisions,[43] and the rate coefficients are obtained using BOLSIG+.[44]

B. Estimation procedure

Recent studies have shown that data assimilation is a useful tool for inverse problems to estimate unknown parameters in several applications.[45–49] In this study, the available measurement data are $n_e(z)$ and $T_e(z)$, and the parameter that we aim to estimate is $\mu_{\mathrm{eff}}(z)$ or $\nu_{ano}(z)$. Interestingly, it can be seen that for this problem, data assimilation techniques, such as Kalman filters, are not necessary.

Each unknown parameter can be estimated by using Eqs. (4)–(9). First, $n_n(z)$ can be uniquely obtained from Eq. (4) assuming that $u_{n,z}$ is constant and $u_{n,z} \approx v_{th,n}$ is the thermal speed. When solving Eq. (4), $n_n(z=0) = \dot{m}_c/(\pi R_0^2 u_{n,z})$ is used as the boundary condition, where $\dot{m}_c$ and R_0 are the cathode mass flow rate and the radius of the orifice exit, respectively. In this study, $R_0 = 4.2$ mm is used. Second, once $n_n(z)$ is obtained, the ionization rate $\dot{n} = k_{iz}(T_e) n_e n_n$ can be determined since n_e and T_e are provided from the LTS measurement, from which $u_{i,z}(z)$ can be obtained by solving Eq. (5). Here, $u_{i,z}(z = 17.75\ \mathrm{mm}) = u_{i,p}$ is specified as the boundary condition. Third, assuming T_i is constant, $E_z(z)$ is obtained from Eq. (6). Fourth, $u_{e,z}(z)$ can be estimated from Eq. (7) assuming the value of A_p. Finally, μ_{eff} and ν_{ano} are evaluated using Eqs. (8) and (9), respectively.

C. Uncertainty quantification

Uncertainty quantification is performed considering both the experimental uncertainty of n_e and T_e shown in Fig. 5 and the assumption uncertainty. In this study, $u_{i,p} \in [2000\ \mathrm{m/s}, 3000\ \mathrm{m/s}]$,[50,51] $T_i \in [0.1\ \mathrm{eV}, 1.0\ \mathrm{eV}]$,[52,53] and $T_n \in [500\ \mathrm{K}, 1500\ \mathrm{K}]$[52,54,55] are considered as the assumed uncertainty ranges based on experimental studies and numerical simulations conducted under similar operating conditions. Note that $u_{i,p} > 0$ is considered based on previous studies of laser-induced fluorescence (LIF) measurements[50,51,56] and a two-dimensional (2D) fluid simulation.[57] For the input to the model, $n_e(z)$ and $T_e(z)$ shown in Fig. 5 are used. The parameters, i.e., $u_{i,p}$, T_i, and T_n, are assigned randomly between the range shown above. Then, the electron mobility is estimated from the model, i.e., Eqs. (4)–(9).

IV. RESULTS

A. Estimated plasma properties

Figure 6 shows the estimated results of (a) $u_{i,z}(z)$, (b) $u_{e,z}(z)$, (c) $E_z(z)$, and (d) $\phi(z) - \phi(z=0)$ in three electrical configurations: grounded, floating, and cathode-tied. Each solid line shows the mean value, and the shadow region shows $\pm 2\sigma$, considering both uncertainties of experimental data and assumptions.

Figure 6(a) shows $u_{i,z}(z) > 0$ due to the large density gradient, as shown in Fig. 5, which is consistent with the literature.[50,51,56,57] Several LIF measurements suggest that the mean velocity (i.e., $u_{i,z}$) is positive from the ion velocity distribution function.[50,51,56] Around $z = 1 - 4$ mm, smaller $u_{i,z}$ is due to larger n_e shown in Fig. 5(a) and the radial diffusion. Figure 6(b) shows that $u_{e,z}$ is on the order of $10^5 - 10^6$ m/s and increases toward the plume. It should be noted that the present study assumes an ambipolar type diffusion in the radial direction, i.e., $u_{e,r} = u_{i,r}$. In Ref. 58, the axial electron velocity $u_{e,z}(z)$ was measured using LTS with the scattering direction aligned along the axial direction. Although those measurements were conducted under standalone operation, $u_{e,z}(z)$ obtained in the present study is in quantitative agreement with the experimental results reported under similar discharge current and mass flow rate conditions. Figure 6(c) shows the electric field, and $|E_z|$ is the smallest for electrical configurations at $z = 0 - 10$ mm due to smaller $|u_i|$ shown in Fig. 6(a). In Fig. 6(d), the relative potential from the orifice potential is obtained from the integration of $E_z(z)$ shown in Fig. 6(c), i.e., $\phi(z) - \phi(z=0) = -\int_0^z E_z(z')dz'$. It should be noted that while the cathode itself has a potential of $V_{cg} = -15$ V, the potential increases due to the plasma potential;[52,59] thus, in this study, we focus only on the potential difference between the cathode exit and plume.

For all cases, $E_z < 0$, i.e., ϕ increases toward the plume, which is consistent with several experimental works[60,61] and 2D fluid simulations.[59,62] More importantly, the potential drop for the grounded configuration is smaller than the floating and cathode-tied configuration. This indicates that the electron can transport

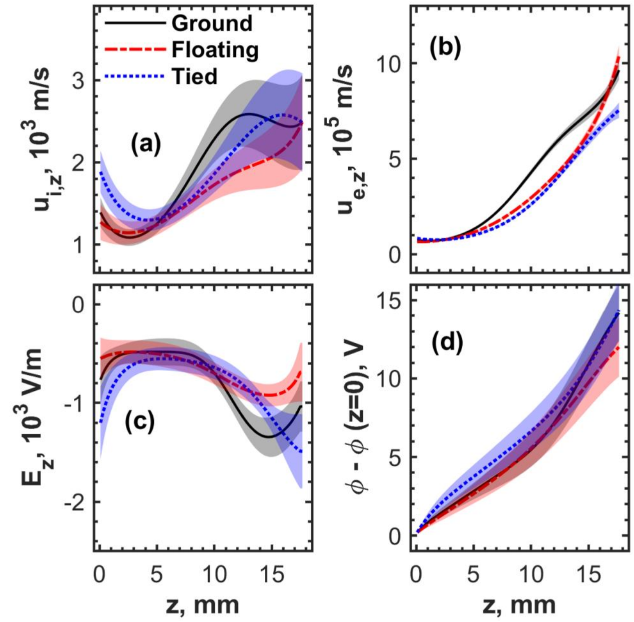

FIG. 6. Estimated results in three electrical configurations: grounded, floating, and cathode-tied. Here, (a) the axial ion bulk velocity, $u_{i,z}(z)$ (b) the axial electron bulk velocity, $u_{e,z}(z)$ (c) the axial electric field, $E_z(z)$ and (d) relative potential with respect to the orifice potential, i.e., $\phi(z) - \phi(z = 0)$. Solid line: mean value, shadow regions 2σ including the uncertainty of the experimental data shown in Fig. 5 and the assumed uncertainty. Note that V_{cg} is -15 V for three electrical configurations.

from the cathode more easily with the grounded configuration for the same discharge current, which will be discussed in Sec. IV C.

B. Anomalous scattering frequency

Figure 7 shows (a) $\mu_{\rm cla}(z)$ and $\mu_{\rm eff}(z)$ and (b) $\nu_{\rm ano}(z)$ for three electrical configurations: grounded, floating, and cathode-tied, where $\mu_{\rm cla} = e/(m_e \nu_m)$ is the classical mobility. $\mu_{\rm cla}(z)$ is on the order of 10^3–$10^4\,{\rm m^2\,V^{-1}\,s^{-1}}$ and increases toward the plume region due to the decreasing neutral density. In contrast, $\mu_{\rm eff}(z)$ is on the order of 10^2–$10^3\,{\rm m^2\,V^{-1}\,s^{-1}}$, which is one to two orders of magnitude smaller than $\mu_{\rm cla}(z)$. This suggests the presence of anomalous electron scattering frequency for the near-field plume of the cathode discharge. It should be noted that we varied the radial diffusion parameter ΔR between 4 and 8 mm and confirmed that the overall trend of $\mu_{\rm eff}$ is similar for three electrical configurations.[41] As shown in Fig. 7(b), $\nu_{\rm ano}(z)$ is on the order of $10^8 - 10^9$ Hz, which quantitatively agrees with the literature.[59,63–65] Several experimental studies have reported the presence of current-driven instabilities (e.g., ion-acoustic turbulence) in hollow cathode discharges.[63,66,67] In the literature, such instabilities are incorporated into fluid models through an anomalous scattering frequency and effective heating source terms for both ions and electrons,[59,62,68] while the present study considers only anomalous electron scattering shown in Eq. (9). In this study, the electron temperature is provided from experimental data, and the effects of electron heating are implicitly accounted for. Ion heating due to such instabilities is not explicitly considered, which represents a limitation of this study. In addition, while the drift-diffusion approximation is used in this study, recent works point out the importance of the electron inertia effects,[42,65,69] which can also contribute to anomalous scattering as the mechanism.[65]

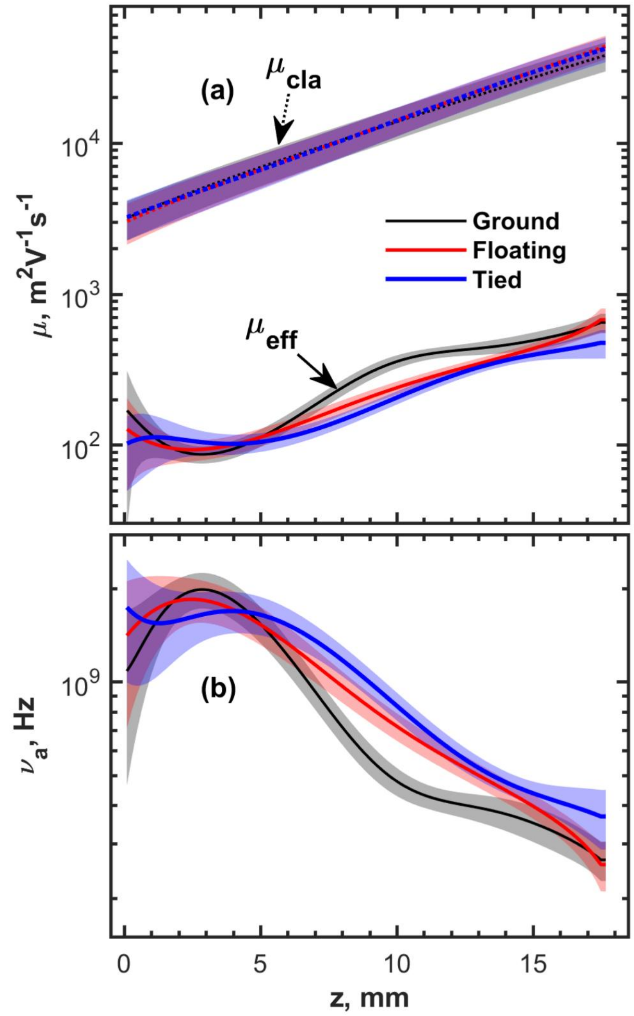

FIG. 7. Estimated properties: (a) $\mu_{\rm eff}(z)$ and $\mu_{\rm cla}(z)$ and (b) $\nu_{\rm ano}(z)$ for three electrical configurations: grounded, floating, and tied. (a) Solid line, mean value of $\nu_{\rm ano}(z)$; dashed line, mean value of $\nu_{\rm cla}(z)$. (b) Solid line, mean value of $\nu_{\rm ano}$. Shadow regions: 2σ including the uncertainty of the experimental data shown in Fig. 5 and the assumed uncertainty.

Figure 8 shows the electron Mach number $M_{e,z}(z) = u_{e,z}(z)/v_{th,e}(z)$, where $v_{th,e}(z)$ is the electron thermal speed. The results show that $M_{e,z}(z) \approx 0.1 - 0.9 < 1$, and $M_e(z)$ increases toward the plume region. In a quasi-linear theory (e.g., Sagdeev model[70]), a larger $M_{e,z}$ corresponds to a stronger instability, i.e., larger $\nu_{\rm ano}$. In

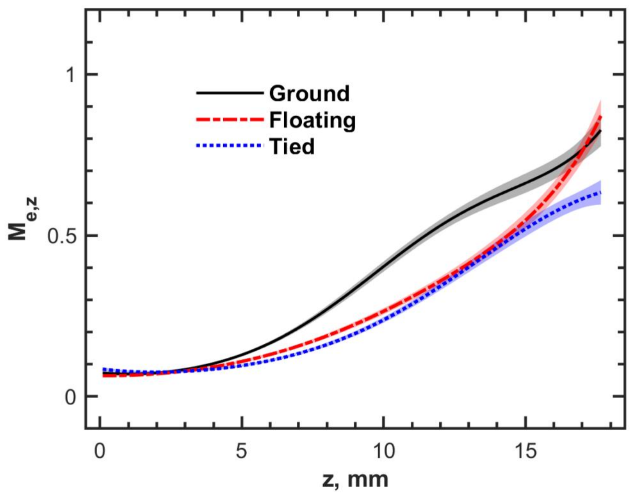

FIG. 8. The electron Mach number obtained from the state estimation for three electrical configurations: grounded, floating, and cathode-tied. Lines: mean value. Shadow regions: $\pm 2\sigma$ of the estimated states.

fact, we confirm that the Sagdeev model used in Ref. 71 predicts the scattering frequency of a similar order of magnitude to ν_{ano} shown in Fig. 7(b); however, the trend toward the plume region is opposite due to $M_{e,z}(z)$ shown in Fig. 8. This discrepancy can be attributed to a nonlinear saturation mechanism of the current-driven instability.[72] A self-consistent kinetic simulation[72] suggests that the initial Mach numbers drive stronger instability, but nonlinear saturation reduces the electron drift velocity and increases the electron temperature, resulting in smaller Mach numbers in the saturated state. Consequently, regions with smaller saturated Mach numbers correspond to stronger instability. Such $M_{e,z} < 1$ is also observed in a recent experiment.[58] Therefore, the spatial variation in $M_{e,z}(z)$ is physically consistent with $\nu_{\text{ano}}(z)$, as shown in Fig. 7(b).

C. Electrical facility effect

Most interestingly, $\mu_{\text{eff}}(z)$ shown in Fig. 7(a), i.e., electron mobility, is the largest around $z = 5 - 15$ mm for the grounded configuration, while μ_{eff} of the floating configuration is comparable to the cathode-tied configuration. Since $V_{tb} = V_{tb,f} \approx -20$ V in the floating condition, a large electron current flows to the ground for the grounded configuration, which likely leads to a large electron conductivity shown in Fig. 7(a). Such an electron flow to the thruster body suppresses the amplitude of discharge current oscillation, as shown in Fig. 2. In the grounded configuration, electrons emitted from the cathode can be collected either by the anode, the thruster body, or the ion beam. Since the discharge power supply is isolated from ground, as shown in Fig. 1, the electron current to the thruster body does not act as the return current of the discharge circuit in the ground configuration. Considering the discharge current is approximately the electron current collected at the anode, electrons diverted to the thruster body reduce the discharge current, which is consistent with the experimental observation. It should be noted that, in the grounded configuration, a global current balance, i.e., zero net current condition, is satisfied in a time-averaged manner between the thruster body and the vacuum chamber. Therefore, if the thruster body locally collects electrons, the chamber sheath potential adjusts so that the chamber walls collect the corresponding ion current. However, in this study, V_{cg} does not change among the electrical configurations. If the coupling between the near-field plume and the far-field plume were strong, a variation in V_{cg} would be expected.[73] The lack of change in V_{cg} therefore suggests that this coupling is limited under the present conditions. Further plume diagnostics (e.g., beam potential) would be useful to clarify this interaction and are reserved for future work.

For the cathode-tied configuration, since $I_{t,e} > I_{t,i}$ (where $I_{t,e}$ and $I_{t,i}$ are the electron and ion current to the thruster body, respectively) due to $V_{tb} = V_{cg} > V_{tb,f}$, the net current $I_{t,e} - I_{t,i}$ can be re-utilized from the cathode. However, in this study, $V_{tb} - V_{cg} \approx -5$ V, which is relatively small; thus, the difference of the electron conductivity between the floating and cathode-tied configurations is not significant, as shown in Fig. 7(a). However, if the cathode is degraded after a long operation, it may be likely that a larger $|V_{cg}|$ is necessary;[26] the difference in the cathode-tied and floating configurations might increase after long-time operation.

If the thruster body is cathode-tied, the CEX ions can be attracted to the thruster body, but the net current does not have to be zero, which is the key difference from the floating configuration. For instance, if the plasma conditions at the sheath edge near the thruster body are similar between different configurations, the smaller sheath potential with a cathode-tied configuration compared to the floating configuration implies that electron current is conducted into the thruster body. In turn, this would mean that the hollow cathode under the cathode-tied configuration needs to conduct slightly higher current than the floating configuration. If the thruster body is connected to the ground and if assuming that the plasma sheath condition is similar between different electrical configurations, the sheath potential near the thruster body for the grounded configuration is even smaller, which can induce large electron current to the thruster body. To prevent that from happening, it is likely that the grounded configuration will adjust the sheath and the bulk plasma to mitigate the electron current flow in the thruster body. While the one-dimensional measurement of n_e and T_e at the cathode exit by incoherent laser Thomson scattering is used in the present study, the two-dimensional measurement of n_e and T_e near the thruster body would be useful to determine more precisely how the plasma sheath structure is changed by the electrical configuration.

V. CONCLUSION

This study investigates how the electrical configuration of the Hall effect thruster body affects the electron transport (cf. electron conductivity) in the near-field hollow cathode plume. The axial profile of the electron density and temperature at the exit of the hollow cathode is obtained from incoherent laser Thomson scattering for three electrical configurations of the thruster body: grounded, floating, and cathode-tied. The LTS measurement show that the electron density and electron temperature are different depending on the electrical configurations. The experimental data of electron density and electron temperature are then input into a one-dimensional fluid model, from which plasma properties are estimated. The results, such as the anomalous electron scattering frequency, are estimated from the model-data fusion framework, qualitatively agreeing with the observations reported in literature. The estimated results suggest that the grounded configuration enhances electron conductivity in the near-cathode plume region, indicating the presence of an electron current path between the cathode exit and the thruster body. Although the plasma diagnostics are limited to a small axial region near the cathode, the electrical configuration produces clear changes in global discharge characteristics, including the mean discharge current and its oscillations. In the grounded configuration, electron collection by the thruster body reduces the current reaching the anode, consistent with the observed decrease in mean discharge current. These results suggest that the near-cathode effects can influence the global discharge behavior and overall thruster performance. Additionally, under both floating and cathode-tied configurations, electron transport appears comparable in this study, indicating that the current path in the near-field region is similar. However, in the cathode-tied configuration, a finite current path exists between the cathode and the thruster body. The difference between the floating and cathode-tied configurations may vary depending on the thruster configuration and the duration of operation. Further multi-dimensional Thomson scattering measurements and data-estimation analyses will enable a more detailed characterization of the electron current path and sheath structure around the thruster body, which is reserved for future work.

ACKNOWLEDGMENTS

This work was supported by NASA through the Joint Advanced Propulsion Institute, a NASA Space Technology Research Institute under Grant No. 80NSSC21K1118.

AUTHOR DECLARATIONS

Conflict of Interest

The authors have no conflicts to disclose.

Author Contributions

Yusuke Yamashita: Conceptualization (equal); Formal analysis (equal); Methodology (lead); Software (equal); Validation (lead); Visualization (lead); Writing – original draft (lead); Writing – review & editing (equal). **Naia Butler-Craig:** Formal analysis (equal); Software (equal); Validation (supporting); Writing – original draft (supporting); Writing – review & editing (equal). **Mitchell L. R. Walker:** Funding acquisition (equal); Project administration (equal); Writing – review & editing (equal). **Kentaro Hara:** Conceptualization (equal); Formal analysis (supporting); Funding acquisition (equal); Methodology (supporting); Project administration (equal); Software (supporting); Validation (supporting); Visualization (supporting); Writing – original draft (supporting); Writing – review & editing (equal).

DATA AVAILABILITY

The data that support the findings of this study are available from the corresponding author upon reasonable request.

REFERENCES

[1]K. Nishiyama, S. Hosoda, R. Tsukizaki, and H. Kuninaka, "In-flight operation of the Hayabusa2 ion engine system on its way to rendezvous with asteroid 162173 Ryugu," Acta Astronaut. **166**, 69–77 (2020).

[2]H. Kuninaka, K. Nishiyama, I. Funaki, Y. Shimizu, T. Yamada, and J. Kawaguchi, "Assessment of plasma interactions and flight status of the HAYABUSA asteroid explorer propelled by microwave discharge ion engines," IEEE Trans. Plasma Sci. **34**, 2125–2132 (2006).

[3]J. R. Brophy, M. D. Rayman, and B. Pavri, "Dawn: An ion-propelled journey to the beginning of the solar system," in *2008 IEEE Aerospace Conference*, No. IEEEAC-2008-1504 (IEEE, 2008).

[4]J. S. Snyder, C. L. Kelly, C. Garner, N. Bradley, I. Johnson, R. Corey, J. B. Ream, and B. P. Weiss, "Initial checkout of the psyche electric propulsion system after launch," in *38th International Electric Propulsion Conference*, No. IEPC-2024-161 (Electric Rocket Propulsion Society, 2024).

[5]I. Funaki, S. Cho, T. Sano, T. Fukatsu, Y. Tashiro, T. Shiiki, Y. Nakamura, H. Watanabe, K. Kubota, Y. Matsunaga *et al.*, "Development of a 6-kW-class Hall thruster for geostationary missions," Acta Astronaut. **170**, 163–171 (2020).

[6]B. R. Frongello, W. A. Hoskins, R. J. Cassady, K. L. Kalkowska, and P. Maliga, "Spacecraft electric propulsion at an inflection point," in *ASCEND 2021*, No. AIAA-2021-4151 (AIAA, 2021).

[7]I. Funaki, S. Cho, T. Sano, T. Fukatsu, Y. Tashiro, T. Shiiki, Y. Nakamura, H. Watanabe, K. Kubota, Y. Matsunaga *et al.*, "1,000-hours demonstration of a 6-kW-class Hall thruster for all-electric propulsion satellite," Trans. Jpn. Soc. Aeronaut. Space Sci. Aerosp. Technol. Jpn. **17**, 589–595 (2019).

[8]H. Kuninaka, K. Nishiyama, I. Funaki, T. Yamada, Y. Shimizu, and J. Kawaguchi, "Powered flight of electron cyclotron resonance ion engines on Hayabusa explorer," J. Propul. Power **23**, 544–551 (2007).

[9]J. Polk, J. Anderson, J. Brophy, V. Rawlin, M. Patterson, J. Sovey, and J. Hamley, "An overview of the results from an 8200 hour wear test of the NSTAR ion thruster," in *35th Joint Propulsion Conference and Exhibit*, No. AIAA-99-2446 (AIAA, 1999).

[10]J. D. Frieman, H. Kamhawi, G. Williams, W. Huang, D. A. Herman, P. Y. Peterson, J. H. Gilland, and R. R. Hofer, "Long duration wear test of the NASA HERMeS Hall thruster," in *2018 Joint Propulsion Conference*, No. AIAA-2018-4645 (AIAA, 2018).

[11]A. Passaro, A. Vicini, F. Nania, and L. Biagioni, "Numerical rebuilding of SMART-1 Hall effect thruster plasma plume," J. Propul. Power **26**, 149–158 (2010).

[12]D. Manzella, R. Jankovsky, F. Elliott, I. Mikellides, G. Jongeward, and D. Allen, "Hall thruster plume measurements on-board the Russian express satellites," in *27th International Electric Propulsion Conference*, No. IEPC-2001-044 (Electric Rocket Propulsion Society, 2001).

[13]J. Polk, R. Kakuda, J. Anderson, J. Brophy, V. Rawlin, J. Sovey, and J. Hamley, "In-flight performance of the NSTAR ion propulsion system on the Deep Space One mission," in *2000 IEEE Aerospace Conference. Proceedings (Cat. No. 00TH8484)*, No. IEEEAC-123 (IEEE, 2000).

[14]J. E. Foster and T. J. Topham, "A review of the impact of ground test-related facility effects on gridded ion thruster operation and performance," Phys. Plasmas **31**, 030501 (2024).

[15]T. Zivre and K. Hara, "Estimation of in-space thruster performance of a Hall effect thruster through extrapolation of plasma states using extended Kalman filter," J. Appl. Phys. **138**, 163305 (2025).

[16]A. L. Ortega, I. G. Mikellides, V. H. Chaplin, J. S. Snyder, and G. Lenguito, "Facility pressure effects on a Hall thruster with an external cathode: I. Numerical simulations," Plasma Sources Sci. Technol. **29**, 035011 (2020).

[17]K. D. Diamant, R. Liang, and R. L. Corey, "The effect of background pressure on SPT-100 Hall thruster performance," in *50th AIAA/ASME/SAE/ASEE Joint Propulsion Conference*, No. AIAA-2014-3710 (AIAA, 2014).
[18]W. Huang and H. Kamhawi, "Facility effects on the ion characteristics of a 12.5-Kilowatt Hall thruster," J. Propul. Power **39**, 665–674 (2023).
[19]M. R. Nakles and W. A. Hargus, Jr., "Background pressure effects on ion velocity distribution within a medium-power Hall thruster," J. Propul. Power **27**, 737–743 (2011).
[20]M. L. R. Walker, A. L. Victor, R. R. Hofer, and A. D. Gallimore, "Effect of backpressure on ion current density measurements in Hall thruster plumes," J. Propul. Power **21**, 408–415 (2005).
[21]D. R. Jovel, J. D. Cabrera, and M. L. R. Walker, "Current pathways model for Hall thruster plumes in ground-based vacuum test facilities: Measurements and observations," Journal of Electric Propulsion **3**, 35 (2024).
[22]R. Shirakawa, Y. Yamashita, D. Koda, R. Tsukizaki, Y. Shimizu, M. Tagawa, and K. Nishiyama, "Investigation and experimental simulation of performance deterioration of microwave discharge ion thruster μ10 during space operation," Acta Astronaut. **174**, 367–376 (2020).
[23]R. B. Lobbia, J. E. Polk, R. R. Hofer, V. H. Chaplin, and B. Jorns, "Accelerating 23,000 hours of ground test backsputtered carbon on a magnetically shielded Hall thruster," in *AIAA Propulsion and Energy 2019 Forum*, No. AIAA-2019-3898 (AIAA, 2019).
[24]J. H. Gilland, G. Williams, J. M. Burt, and J. Yim, "Carbon back sputter modeling for Hall thruster testing," in *52nd AIAA/SAE/ASEE Joint Propulsion Conference*, No. AIAA-2016-4941 (AIAA, 2016).
[25]J. A. Walker, J. D. Frieman, M. L. R. Walker, V. Khayms, D. King, and P. Y. Peterson, "Electrical facility effects on Hall-effect-thruster cathode coupling: Discharge oscillations and facility coupling," J. Propul. Power **32**, 844–855 (2016).
[26]A. Nono, T. Morishita, S. Hosoda, R. Tsukizaki, and K. Nishiyama, "Effect of spacecraft surface conductivity on voltage of microwave neutralizer in gridded ion thrusters," Acta Astronaut. **212**, 130–138 (2023).
[27]K. Nishiyama, R. Tsukizaki, S. Imai, T. Morishita, T. Kuniyoshi, and Y. Yamashita, "Ion engine operation during Hayabusa2 extended mission before the flyby with asteroid 2001 CC21," in *39th International Electric Propulsion Conference*, No. IEPC-2025-572 (Electric Rocket Propulsion Society, 2025).
[28]R. Tsukizaki, R. Shirasawa, M. R. Inchingolo, T. Morishita, and K. Nishiyama, "Experimental investigation of anomalous sputtering in the vicinity of microwave neutralizer cathode by laser-induced fluorescence spectroscopy," in *38th International Electric Propulsion Conference*, No. IEPC-2024-545 (Electric Rocket Propulsion Society, 2024).
[29]P. Y. Peterson, H. Kamhawi, W. Huang, G. Williams, J. H. Gilland, J. Yim, R. R. Hofer, and D. A. Herman, "NASA's Hermes Hall thruster electrical configuration characterization," in *52nd AIAA/SAE/ASEE Joint Propulsion Conference*, No. AIAA-2016-5027 (AIAA, 2016).
[30]N. I. Butler-Craig, J. L. Suazo Betancourt, J. Lopez-Uricoechea, D. Lev, and M. L. R. Walker, "Comparison of the near-field electron properties of the H9 Hall effect thruster in various electrical configurations with incoherent laser Thomson scattering," in *AIAA SCITECH 2025 Forum*, No. AIAA-2025-1099 (AIAA, 2025).
[31]J. D. Frieman, J. A. Walker, M. L. R. Walker, V. Khayms, and D. Q. King, "Electrical facility effects on Hall thruster cathode coupling: Performance and plume properties," J. Propul. Power **32**, 251–264 (2016).
[32]D. R. Jovel, J. D. Cabrera, and M. L. R. Walker, "Hall effect thruster impedance characterization in ground-based vacuum test facilities," J. Electric Propuls. **3**, 1–26 (2024).
[33]R. R. Hofer, S. E. Cusson, R. B. Lobbia, and A. D. Gallimore, "The H9 magnetically shielded Hall thruster," in *35th International Electric Propulsion Conference*, No. IEPC-2017-232 (Electric Rocket Propulsion Society, 2017).
[34]J. Walker, D. Lev, M. L. R. Walker, V. Khayms, and D. King, "Electrical characteristics of a Hall effect thruster body in a vacuum facility testing environment," J. Electric Propuls. **1**, 18 (2022).
[35]H. Watanabe, S. Cho, K. Kubota, G. Ito, K. Fuchigami, K. Uematsu, Y. Tashiro, S. Iihara, and I. Funaki, "Performance evaluation of a two-kilowatt magnetically shielded Hall thruster," J. Propul. Power **36**, 14–24 (2020).
[36]J. L. S. Betancourt, N. Butler-Craig, J. Lopez-Uricoechea, A. M. Steinberg, and M. L. R. Walker, "Laser Thomson scattering measurements indicate non-isothermal magnetic field lines in magnetically shielded Hall effect thrusters," Phys. Plasmas **31**, 113106 (2024).
[37]J. Lopez-Uricoechea, J. L. Suazo Betancourt, N. Butler-Craig, and M. L. R. Walker, "Spatially resolved Thomson scattering measurements of electron properties across the acceleration region of a high-power magnetically shielded Hall effect thruster," J. Appl. Phys. **136**, 113303 (2024).
[38]J. L. Suazo Betancourt, N. Butler-Craig, J. Lopez-Uricoechea, J. Bak, D. Lee, A. M. Steinberg, and M. L. R. Walker, "Thomson scattering measurements in the krypton plume of a lanthanum hexaboride hollow cathode in a large vacuum test facility," J. Appl. Phys. **135**, 083302 (2024).
[39]B. Vincent, S. Tsikata, and S. Mazouffre, "Incoherent Thomson scattering measurements of electron properties in a conventional and magnetically-shielded Hall thruster," Plasma Sources Sci. Technol. **29**, 035015 (2020).
[40]N. I. Butler-Craig, "Experimental investigation of varied thruster body bias on electron behavior in the near-field of a magnetically shielded Hall thruster," Ph.D. thesis (Georgia Institute of Technology, 2026).
[41]Y. Yamashita, N. Butler-Craig, M. L. R. Walker, and K. Hara, "Electron mobility estimation of hollow cathode plasma in different electrical configurations," in *39th International Electric Propulsion Conference*, No. IEPC-2025-455 (Electric Rocket Propulsion Society, 2025).
[42]K. Hara, "An overview of discharge plasma modeling for Hall effect thrusters," Plasma Sources Sci. Technol. **28**, 044001 (2019).
[43]See www.lxcat.net/Biagi-v7.1 for "Biagi-v7.1 database" (last accessed August 2023).
[44]G. J. M. Hagelaar and L. C. Pitchford, "Solving the Boltzmann equation to obtain electron transport coefficients and rate coefficients for fluid models," Plasma Sources Sci. Technol. **14**, 722 (2005).
[45]B. Jorns, "Predictive, data-driven model for the anomalous electron collision frequency in a Hall effect thruster," Plasma Sources Sci. Technol. **27**, 104007 (2018).
[46]A. Dwivedi, M. Cerepi, and K. Hara, "Spatiotemporal state and parameter estimation of plasma dynamics using data assimilation," Phys. Plasmas **32**, 063509 (2025).
[47]A. Dwivedi and K. Hara, "Estimation of electron kinetics in low-temperature plasmas using data assimilation," J. Phys. D: Appl. Phys. **58**, 175203 (2025).
[48]D. E. Troyetsky, C. M. Greve, S. Tsikata, and K. Hara, "State estimation of the dynamic behavior of plasma properties in a Hall effect thruster discharge," J. Phys. D: Appl. Phys. **56**, 444001 (2023).
[49]C. M. Greve, M. Majji, and K. Hara, "Real-time state estimation of low-frequency plasma oscillations in Hall effect thrusters," Phys. Plasmas **28**, 093509 (2021).
[50]G.-C. Potrivitu, S. Mazouffre, L. Grimaud, and R. Joussot, "Anode geometry influence on LaB_6 cathode discharge characteristics," Phys. Plasmas **26**, 113506 (2019).
[51]G. J. Williams, T. B. Smith, M. T. Domonkos, A. D. Gallimore, and R. P. Drake, "Laser-induced fluorescence characterization of ions emitted from hollow cathodes," IEEE Trans. Plasma Sci. **28**, 1664–1675 (2000).
[52]G. Sary, L. Garrigues, and J.-P. Boeuf, "Hollow cathode modeling: II. Physical analysis and parametric study," Plasma Sources Sci. Technol. **26**, 055008 (2017).
[53]C. A. Dodson, D. Perez-Grande, B. A. Jorns, D. M. Goebel, and R. E. Wirz, "Ion heating measurements on the centerline of a high-current hollow cathode plume," J. Propul. Power **34**, 1225–1234 (2018).
[54]J. Polk, C. Marrese-Reading, B. Thornber, L. Dang, L. Johnson, and I. Katz, "Scanning optical pyrometer for measuring temperatures in hollow cathodes," Rev. Sci. Instrum. **78**, 093101 (2007).
[55]Y. Oshio, K. Hirai, H. Watanabe, H. Horisawa, and I. Funaki, "Orifice plate surface temperature measurement of a LaB_6 hollow cathode using a near-infrared two-color radiation thermometer," J. Electric Propuls. **3**, 33 (2024).

[56] C. Dodson, B. Jorns, and R. Wirz, "Measurements of ion velocity and wave propagation in a hollow cathode plume," Plasma Sources Sci. Technol. **28**, 065009 (2019).
[57] I. G. Mikellides, D. M. Goebel, B. A. Jorns, J. E. Polk, and P. Guerrero, "Numerical simulations of the partially ionized gas in a 100-A LaB_6 hollow cathode," IEEE Trans. Plasma Sci. **43**, 173–184 (2015).
[58] P. Roberts, Z. Brown, and B. Jorns, "Hollow cathode electron properties are consistent with marginally stable turbulence," Appl. Phys. Lett. **126**, 074103 (2025).
[59] A. L. Ortega, B. A. Jorns, and I. G. Mikellides, "Hollow cathode simulations with a first-principles model of ion-acoustic anomalous resistivity," J. Propul. Power **34**, 1026–1038 (2018).
[60] D. M. Goebel, K. K. Jameson, I. Katz, and I. G. Mikellides, "Potential fluctuations and energetic ion production in hollow cathode discharges," Phys. Plasmas **14**, 103508 (2007).
[61] I. G. Mikellides, I. Katz, and D. M. Goebel, "Numerical simulation of the hollow cathode discharge plasma dynamics," in *29th International Electric Propulsion Conference*, No. IEPC-2005-200 (Electric Rocket Propulsion Society, 2005).
[62] G. Sary, L. Garrigues, and J.-P. Boeuf, "Hollow cathode modeling: I. A coupled plasma thermal two-dimensional model," Plasma Sources Sci. Technol. **26**, 055007 (2017).
[63] M. P. Georgin, B. A. Jorns, and A. D. Gallimore, "Transient non-classical transport in the hollow cathode plume I: Measurements of time-varying electron collision frequency," Plasma Sources Sci. Technol. **29**, 105010 (2020).
[64] M. P. Georgin and B. A. Jorns, "Transient non-classical transport in the hollow cathode plume II: Evaluation of models for the anomalous collision frequency," Plasma Sources Sci. Technol. **29**, 105011 (2020).
[65] M. P. Georgin and M. S. McDonald, "Experimental evaluation of the 2D non-classical ohmic transport model for electrons in the hollow cathode plume," J. Appl. Phys. **130**, 203301 (2021).
[66] G.-C. Potrivitu and S. Xu, "Evidence of the ionization instability and ion acoustic turbulence correlation in sub-ampere hollow cathodes," J. Electric Propuls. **1**, 6 (2022).
[67] B. A. Jorns, I. G. Mikellides, and D. M. Goebel, "Ion acoustic turbulence in a 100-A LaB_6 hollow cathode," Phys. Rev. E **90**, 063106 (2014).
[68] T. A. Marks and B. A. Jorns, "Challenges with the self-consistent implementation of closure models for anomalous electron transport in fluid simulations of Hall thrusters," Plasma Sources Sci. Technol. **32**, 045016 (2023).
[69] R. Sahu, A. R. Mansour, and K. Hara, "Full fluid moment model for low temperature magnetized plasmas," Phys. Plasmas **27**, 113505 (2020).
[70] R. Z. Sagdeev and A. A. Galeev, *Nonlinear Plasma Theory* (W. A. Benjamin, New York, 1969).
[71] I. G. Mikellides, I. Katz, D. M. Goebel, and J. E. Polk, "Hollow cathode theory and experiment. II. A two-dimensional theoretical model of the emitter region," J. Appl. Phys. **98**, 113303 (2005).
[72] K. Hara and C. Treece, "Ion kinetics and nonlinear saturation of current-driven instabilities relevant to hollow cathode plasmas," Plasma Sources Sci. Technol. **28**, 055013 (2019).
[73] J. D. Frieman, S. T. King, M. L. Walker, V. Khayms, and D. King, "Role of a conducting vacuum chamber in the Hall effect thruster electrical circuit," J. Propul. Power **30**, 1471–1479 (2014).